

A *NICER* and *AstroSat* view of the neutron star low-mass X-ray binary 1A 1246–588

Vaidehi Poojyam^{a,b,1,*}, Vikas Mistry^{b,2}, Yash Bhargava^{c,d,3}, Sudip
Bhattacharyya^{c,4}, Nitinkumar Bijewar^b

^a*Department of Physics and Astronomy, University of Alabama, Tuscaloosa, AL, USA*

^b*Department of Physics, University of Mumbai, Mumbai, India*

^c*Department of Astronomy and Astrophysics, Tata Institute of Fundamental
Research, Mumbai, India*

^d*INAF-Osservatorio Astronomico di Cagliari, Selargius, Italy*

Abstract

Neutron star (NS) low-mass X-ray binary (LMXB) systems depict a variety of X-ray spectral and timing features, which can be useful to probe the accretion-ejection mechanism in the strong gravity regime. Here, we study the relatively unexplored and faint NS LMXB 1A 1246–588, which is also an ultra-compact X-ray binary (UCXB) with a white dwarf donor. We investigate its temporal and spectral behavior using pointed *NICER* and *AstroSat* observations, supported by long-term *MAXI*/GSC monitoring. The *MAXI* light curve shows modest, recurrent outburst-like enhancements, providing the long-term flux context for interpreting the pointed observations. During the *AstroSat* observations in 2017, the source exhibits an absorbed 0.4–20 keV flux of $(1.18 \pm 0.02) \times 10^{-10}$ erg cm⁻² s⁻¹, while during the *NICER* observations in 2019 it spans an absorbed 0.5–10 keV flux range of $(0.7\text{--}3.7) \times 10^{-10}$ erg cm⁻² s⁻¹ and traces an atoll-like pattern in the hardness–intensity diagram. Broadband spectral modeling shows that the emission is well described by a soft blackbody and a hard Comptonized component, with no statistically required multicolor disk contribution. The

*Corresponding author.

Email address: <vaidehi.poojyam15@gmail.com> (Vaidehi Poojyam)

¹ORCID: 0009-0006-5654-1473

²ORCID: 0009-0009-6459-0728

³ORCID: 0000-0002-5967-8399

⁴ORCID: 0000-0002-6351-5808

blackbody temperature increases from 0.28 to 0.39 keV, with an emitting radius consistent within 6.9–13.8 km, while the Comptonization photon index varies from 1.8 to 2.3. We find that the observed spectral-state evolution is driven by a redistribution of accretion power between thermal emission from the NS boundary layer and Comptonized emission, consistent with atoll-type behavior. These results provide the first quantitative, multi-epoch view of accretion-state evolution in 1A 1246–588, revealing systematic changes in the thermal boundary-layer emission and the Comptonizing region in this UCXB system.

Keywords: Low-mass X-ray binaries, accretion, neutron stars, *NICER*, *AstroSat*

1. Introduction

Low-mass X-ray binaries (LMXBs) are stellar systems with a low-mass ($\lesssim 1M_{\odot}$) donor/companion star and a compact object, the latter being either a black hole (BH) or a neutron star (NS). In an LMXB, the donor star fills its Roche lobe and its matter flows through the inner Lagrangian point to the compact object via an accretion disk (Bhattacharya and van den Heuvel, 1991). The donor can fill its Roche lobe when its radius increases due to evolution or irradiation, or if the Roche lobe size decreases when the binary orbit shrinks. The latter case is common for ultra-compact X-ray binaries (UCXBs), which have a typical period of $\lesssim 80$ min and have a dwarf donor star. In most cases, a UCXB hosts an NS as the compact object (see Armas Padilla, M. et al., 2023, for a complete list of known UCXBs to date). In NS LMXBs, the classification of spectral states is traditionally based on the source trajectories in hardness–intensity and color–color diagrams and the relative dominance of spectral components. Based on the shape traced on their hardness-intensity diagrams (HID) or color-color diagrams (CCD), the NS LMXBs are roughly classified into two types: Z sources and atoll sources (Hasinger and van der Klis, 1989). Z sources accrete at a higher accretion rate with an X-ray luminosity of $\gtrsim 0.5 L_{Edd}$ and trace a Z-shaped track in their HID or CCD. Atoll sources span a broader range of luminosities, typically between $10^{-3} L_{Edd}$ and $0.5 L_{Edd}$ (van der Klis, 2004; Done et al., 2007). Most of the atoll sources are characterized by two distinct tracks in their HIDs and CCDs, a banana-like structure and isolated patches called island states (Hasinger and van der Klis, 1989; van der Klis, 2004;

Church et al., 2006). Furthermore, the banana branch is often divided into upper and lower banana based on their hardness and intensity, and these two states exhibit different spectral and timing properties (Hasinger and van der Klis, 1989; van der Klis, 2004). Within this broader phenomenology, the standard LMXB spectral frameworks offer two widely used interpretations. In the *Eastern* model (Mitsuda et al., 1984, 1989), the soft X-ray emission arises from a multi-temperature accretion disk, while the hard component is produced by Comptonization in the inner disk region. In contrast, the *Western* model (Mitsuda et al., 1984; White et al., 1988) attributes the soft emission to blackbody radiation from the neutron star surface or boundary layer, with the hard component generated in an optically thick Comptonizing region associated with the boundary layer.

1A 1246–588 is a relatively poorly studied LMXB, which was discovered as a persistent X-ray source in the Ariel survey (Carpenter et al., 1977). The source underwent thermonuclear X-ray bursts that last about ~ 150 s (Piro et al., 1997; Boller et al., 1997; in’t Zand et al., 2008), confirming that the compact object is an NS. Bassa et al. (2006) identified the companion star in the system as a white dwarf (WD), strongly suggesting that 1A 1246–588 is a UCXB (Asai et al., 2022), although the orbital period is still unknown (in’t Zand et al., 2008). The distance of the source based on the optical properties has been estimated to be about 4.3 kpc (in’t Zand et al., 2008). The source has also shown kilohertz (kHz) quasi-periodic oscillations (QPO) at ~ 1260 Hz (Jonker et al., 2007; van Doesburgh et al., 2018). in’t Zand et al. (2008) investigated the nature of bursts and the persistent emission using observations from *BeppoSAX*, *RXTE/PCA*, *Swift/XRT*, and *XMM-Newton*. The authors reported that the regular PCA monitoring of the source demonstrates low and high flux states that differ in spectral composition. The 3–20 keV spectra from *RXTE/PCA* of the low state were modeled sufficiently with a power-law-like emission, and the high-state emission in 0.3–20 keV (*Swift/XRT* and *RXTE/PCA*) showed a significant high-energy cutoff and was modeled as an absorbed Comptonization ($kT_e \approx 2.4$ keV) with an absorption column density of 2.1×10^{21} cm $^{-2}$. The long-term ASM light curve of 1A 1246–588 binned at 7 days showed aperiodic variations at time scales of ~ 100 days (in’t Zand et al., 2008), and the weekly PCA monitoring hinted that these long-term variations relate to the high and low states of the source. Asai et al. (2022) modeled the long-term variation of the source and interpreted the quasi-periodic variation at time scales of years as various slow mass-transfer processes from donor to the compact object (e.g., variation in

the mass-transfer rate, variation in the irradiation from the compact object to the donor, etc.).

A key question that remains unexplored for 1A 1246–588 is how its soft X-ray spectral properties evolve on day timescales, something that earlier broadband studies could not resolve. Neutron Star Interior Composition Explorer’s (*NICER*) sensitivity in the 0.5–10 keV band allows us to track these short-term spectral changes and connect them to the source’s accretion state evolution. *AstroSat* observations provide complementary broadband coverage with its simultaneous Soft X-ray Telescope (SXT; 0.3–8 keV) and Large Area X-ray Proportional Counter (LAXPC; 3–80 keV) observations, allowing us to probe the hard X-ray spectral shape and place constraints on the presence of high-energy cutoffs that are inaccessible to *NICER*. Even when the hard X-ray statistics are limited, the *AstroSat* data help place the *NICER* soft X-ray spectral evolution in the context of the source’s overall accretion state. In this paper, we characterize the evolution of the spectral properties of 1A 1246–588 using *NICER* (2019) and *AstroSat* (2017) observations and interpret these changes in the context of the long-term, recurrent variability revealed by the Monitor of All-sky X-ray Image (*MAXI*; Matsuoka et al. (2009)). In Section 2, we describe the observation and data reduction methods used to extract the spectral products. In Section 3, we detail the analysis methods, and in Section 4 and 5, we discuss the results and interpret our findings.

2. Observation and Data reduction

2.1. *NICER*

NICER (Gendreau et al., 2016) X-ray Timing Instrument (XTI; Arzoumanian et al., 2014) observed 1A 1246–588 over a span of 72 days from 21 November, 2019 to 31 January, 2020. The corresponding observation IDs are listed in Table 1. For our analysis, we use data in the 0.5–10 keV range, consistent with the well-calibrated energy band of the *NICER*-XTI. Data reduction and extraction of spectral and timing products are performed using the *NICER* CALDB version `xTi20240206`. Data from detectors 14 and 34 were excluded from the analysis owing to their known elevated instrumental noise. Observations with a net exposure time shorter than or equal to 50 s (e.g., ObsID 2200970127; see Table 1) were excluded from further analysis, as such exposures do not provide sufficient statistics for reliable spectral or timing measurements. The raw level 1 data are processed into

level 2 event files using the `nicer12` pipeline. Spectra and associated Response Matrix File (RMF) and Ancillary Response File (ARF) are extracted using `nicer13-spect`, while light curves across various energy bands are generated with `nicer13-lc`. To model and subtract the background, we employ the SCORPEON model (NASA/GSFC 2023)⁵ which accounts for the non X-ray background and the cosmic X-ray background, utilizing the appropriate file-based background estimator. Preliminary light curves reveal occurrences of apparent flaring activity. To determine whether these are instrumental in origin, such as precipitation electron flares, we examine the high-energy (8–12 keV) intensity, overshoot rate, and the geomagnetic cut-off rigidity parameter (`COR_SAX`)⁶. Noting a correlation, we exclude intervals with `COR_SAX` < 1.5 GeV/c and eliminate the flaring features, thereby confirming their instrumental nature. Following the removal of flaring intervals, all light curve and spectral products are re-extracted. The light curve for one of the observations (ObsID 2200970129) depicts a thermonuclear burst-like structure. As the primary focus of the work is the persistent emission properties of 1A 1246–588 in the soft X-rays, we exclude this observation from our analysis; however, such bursts have been reported for 1A 1246–588 (Piro et al., 1997; Boller et al., 1997; in’t Zand et al., 2008). The final background-subtracted light curve is shown in Figure 1. For normalization purposes, the intensities are scaled relative to the Crab, using data from a *NICER* observation conducted on 26 November, 2019 (ObsID 2205010101).

2.2. *AstroSat*

AstroSat (Singh et al., 2014) observed 1A 1246–588 from 8 April, 2017 to 9 April, 2017 (observation ID G07_065T02_9000001150). The details of the observation are mentioned in the Table 1. We use the data from two primary instruments aboard *AstroSat*: the Soft X-ray Telescope (SXT; Singh et al., 2016, 2017) and the Large Area X-ray Proportional Counter (LAXPC; Yadav et al., 2016, 2017). We investigate the spectral properties of the source in 0.4–20 keV, where the SXT calibration is robust and the LAXPC signal is not dominated by background, using the data products extracted from the SXT and LAXPC instruments. In order to compare the source properties during the epochs of *AstroSat* and *NICER* observations, we normalize the intensity

⁵https://heasarc.gsfc.nasa.gov/docs/nicer/analysis_threads/scorpeon-overview/

⁶https://heasarc.gsfc.nasa.gov/docs/nicer/analysis_threads/flares/

using a nearby Crab observation (observation ID A02_090T01_9000000970 taken on 21 January, 2017). No thermonuclear bursts are detected during the *AstroSat* observation, indicating that the source remains in a persistent, non-bursting state throughout this epoch.

2.2.1. SXT

SXT level 2 data are downloaded from the Indian Space Science Data Centre (ISSDC) data archive. The data from multiple orbits are merged using the Julia tool `sxtevtmergerj1`⁷. For the analysis, a region of 15' centered on the source is selected using `ds9`, and the `xselect` tool is used to extract the light curve and spectrum of the source. The exposure time of SXT is 25.22 ks with a net intensity of 1.363 ± 0.007 counts s⁻¹. At these intensities, pile-up effects are negligible, and thus we use a circular region for extraction. The `sxtARFModule` tool is utilized to modify the standard ARF supplied by the SXT Payload Operation Centre (POC), and the spectrum is grouped according to the detector response using `ftgrouppha`. The standard response and background files provided by the SXT POC are used for the analysis. The SXT spectrum is restricted to 0.4–7.0 keV because of calibration uncertainties at lower energies and poor signal-to-noise at higher energies, where the effective area declines sharply.

2.2.2. LAXPC

The level 1 LAXPC data are processed and converted to level 2 data using the `laxpc_make_event` tool from the pipeline `LAXPCsoftware22Aug15`⁸, with the standard filtering applied to exclude the South Atlantic Anomaly and the Earth occultation intervals using the `laxpc_make_stdgti` tool. We extract spectra from LXP10 and LXP20 as the LXP30 unit had a gas leak early in the mission. The LAXPC observation is background dominated, and thus we extract the spectrum and the background spectrum using the faint source procedure described in Misra et al. (2021) and Antia et al. (2022), which only considers the intervals in which the background is well behaved. We extract the spectra from layer 1 for both units, as it has the lowest background. The LAXPC spectra are logarithmically re-binned to account for the detector energy resolution and other variability components. The spectrum extraction tool in `LAXPCsoftware22Aug15` also generates a suitable response matrix for

⁷https://www.tifr.res.in/~astrosat_sxt/dataanalysis.html

⁸<http://astrosat-ssc.iucaa.in/laxpcData>

Table 1: *NICER* and *AstroSat* observation log for 1A 1246–588.

Telescope	Instrument	ObsID	MJD start	Exposure (ks)
<i>NICER</i>	XTI	2200970101	58808.139	4.81
		2200970102	58809.170	4.22
		2200970103	58810.008	9.16
		2200970104	58811.046	5.11
		2200970105	58812.072	2.10
		2200970106	58813.171	3.72
		2200970107	58814.008	4.60
		2200970108	58815.245	3.38
		2200970122	58833.946	0.87
		2200970123	58834.010	2.59
		2200970124	58838.064	2.88
		2200970125	58843.045	0.46
		2200970126	58847.363	0.77
		2200970127	58849.536	0.05
		2200970128	58850.502	2.72
		2200970130	58851.994	4.14
		2200970131	58853.207	2.95
		2200970132	58854.434	1.92
		2200970133	58855.400	1.77
		2200970134	58856.369	2.49
2200970136	58858.046	1.38		
2200970137	58859.077	1.75		
2200970138	58860.174	2.37		
2200970139	58861.270	1.57		
2200970140	58862.883	3.53		
2200970141	58863.270	3.52		
2200970142	58872.187	1.35		
2200970143	58879.650	0.59		
<i>AstroSat</i>	SXT	G07_065T02_9000001150	57851.831	25.22
	LAXPC			40.30

each spectrum. The exposure time for both LAXPC units is 40.3 ks with a intensity of 8.27 ± 0.29 counts s^{-1} and 7.33 ± 0.07 counts s^{-1} for LXP10 and LXP20, respectively.

2.3. *MAXI light curve*

To investigate the long-term evolution of 1A 1246–588, we refer to the *MAXI* (Matsuoka et al., 2009) light curve of the source in the full energy band (2–20 keV) and two of the softer bands (2–4 keV and 4–10 keV). The standard background-subtracted light curves are procured from the *MAXI-Riken* website⁹. We depict the full-band light curve in different panels of Figure 2. Since the source is faint during its persistent state, the standard background-subtracted light curve may have over-subtraction in some of the energy bands, and thus the time bins where the estimated rate is either negative or consistent with zero within 1σ are excluded from the plotting.

3. Data analysis

3.1. *Lightcurve and HID analysis*

To place the pointed observations in a broader flux context, we begin with the long-term *MAXI* light curve (Figure 2), which shows modest, recurrent rises in the 2–20 keV daily rate but no coherent periodicity. These variations establish the overall activity level of the source and mark the epochs during which the *NICER* and *AstroSat* observations were obtained. We extract background-subtracted *NICER* lightcurves with 100 s bins (Figure 1) for all observations. For *AstroSat*-LAXPC, the background-subtracted lightcurve and HID are constructed using LAXPC units LXP10 and LXP20. To place both instruments on the same hardness-intensity space, we construct HIDs from background subtracted, Crab normalized lightcurves in a soft band of 3–5 keV, a hard band of 5–10 keV, and a full band of 3–10 keV; hardness is defined as $(5\text{--}10 \text{ keV}) / (3\text{--}5 \text{ keV})$ (Figure 3). The *AstroSat* epoch is indicated by a black triangle. Colors and markers are kept identical across Figures 1 and 3; each ObsID 22009701XX is represented by the same symbol/color in both. Throughout the *NICER* campaign, the source varies strongly on short timescales, alternating between quiescent stretches and brief flares that peak at the highest 3–10 keV intensity observed (Figure 1). Two bright intervals

⁹http://maxi.riken.jp/star_data/J1249-590/J1249-590.html

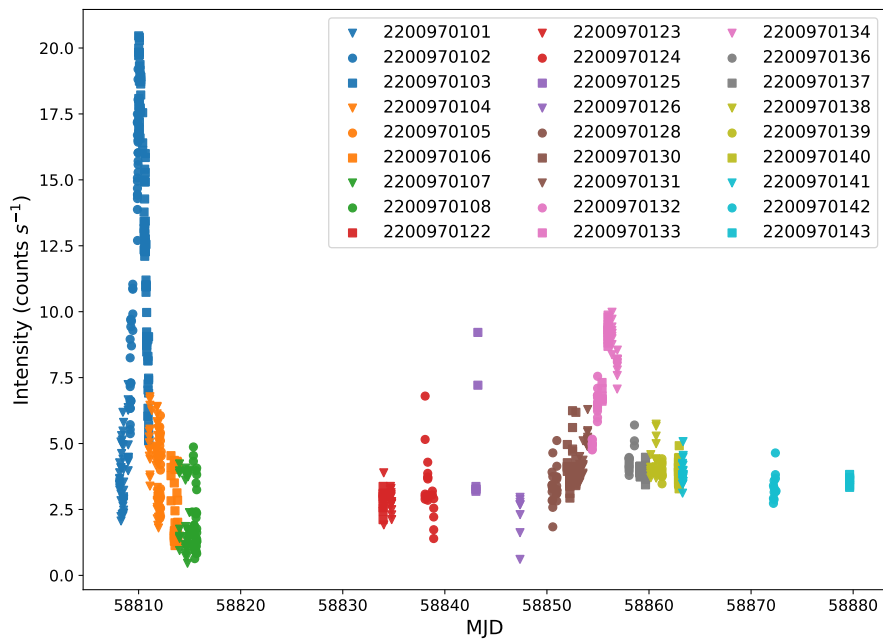


Figure 1: Background-subtracted light curve of 1A 1246–588 in 3–10 keV as observed by *NICER* (see Section 3.1). The observations are binned at 100 s. Each observation is color-coded, as indicated in the legend. The details of the observations are mentioned in the Table 1. The source displays pronounced intensity variability, alternating between distinct high and low-flux intervals over the course of the *NICER* campaign.

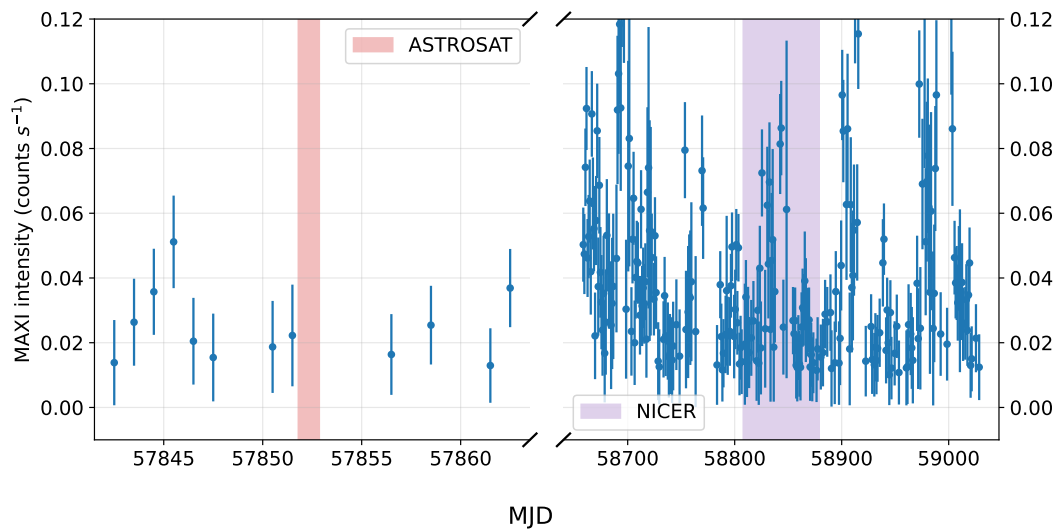


Figure 2: Long-term *MAXI* light curves of 1A 1246–588 (see Section 2.3). The *MAXI* intensities are in 2–20 keV with one-day time bins with 1σ errors. The broken x -axis separates a zoom around the *AstroSat* epoch (left) from a broader view that includes the *NICER* campaign (right). Shaded bands mark the *AstroSat* (red) and *NICER* (violet) observation windows. This plot places the pointed observations in their long-term context and shows that 1A 1246–588 remains persistently active with modest variability during both intervals.

are particularly prominent; an early phase (e.g., ObsIDs 2200970102–0103; blue symbols) and a later bright phase (e.g., 2200970133–0134; pink symbols), separated by intermediate states with stable, lower intensity. In the HID, both *NICER* epochs follow a track consistent with the atoll “banana” branch (Hasinger and van der Klis, 1989). The second bright interval (pink points), corresponding to the second peak in the *NICER* light curve, largely retraces this shape, showing that similar spectral states are reached at different flux levels. This HID behavior guides our spectral analysis, allowing us to group observations by hardness and select representative intervals for time-resolved spectroscopy (Section 3.2).

3.2. Spectral analysis

We analyze the *AstroSat* (SXT+LAXPC) and the *NICER* spectra of 1A 1246–588 using the `xspec` software package (version 12.14.0), adopting χ^2 statistics, and report all confidence intervals at the 1σ level. We generally limit the energy intervals to 0.4–7 keV for the SXT spectrum, 3–20 keV for the LAXPC spectrum, and 0.5–10 keV for the *NICER* spectra, although some *NICER* spectra require reduced energy ranges due to stronger background contamination at higher energy ranges. The SXT spectrum is corrected for gain uncertainties in the response matrix by fitting the gain offset, which is 45 ± 3 eV. The observed count spectrum for SXT-LAXPC and *NICER* are shown in panels (a) and (d) of Figure 4, respectively. Because the SXT+LAXPC intensity is relatively low and the spectra are not systematics dominated, we do not include any additional systematic uncertainties. Similarly, no systematic uncertainty is applied to the *NICER* spectra, as the inclusion of the standard recommended systematic error leads to over-fitting and suppresses statistically significant residuals. In most *NICER* spectra, there is an extra residual at lower energies (≈ 0.75 keV), commonly attributed to calibration uncertainties associated with the oxygen K-edge and the soft X-ray detector response (e.g. Ludlam et al., 2018; Bogdanov et al., 2019). We model this feature using a (`gaussian`) component with the centroid energy fixed at 0.75 keV and the width fixed at 0.05 keV, following standard practice in *NICER* analyses (e.g. Zhang et al., 2023; Putha et al., 2024).

We begin with the *NICER* spectral modeling and then discuss the SXT-LAXPC spectra in that framework. Given that the source is stable within the typical short durations of *NICER* we model individual observations independently. As a representative case, we describe the spectral modeling of ObsID 2200970103, which has one of the highest intensities (21 counts s⁻¹)

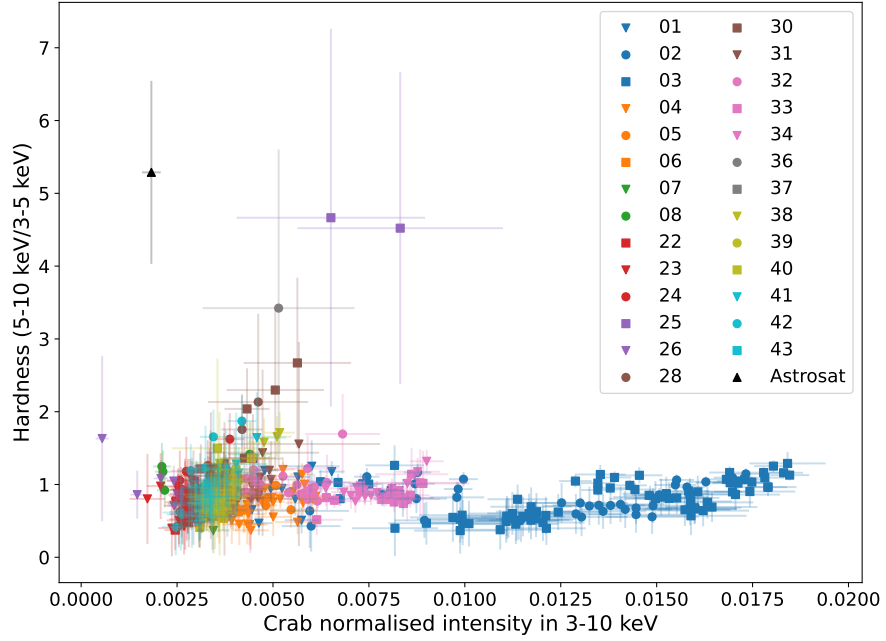


Figure 3: Hardness-intensity diagram (HID) of 1A 1246–588 using the *AstroSat* and *NICER* background-subtracted and Crab-normalized light curves in soft band: 3–5 keV, hard band: 5–10 keV, and full band: 3–10 keV (see section 3.1). The color, marker coding, and the binning for the HID are kept identical to Figure 1. The epoch of the *AstroSat* observation is indicated with a black triangle. In the legend, the two digits correspond to the observation ID 22009701XX to improve the clarity of the plot. This HID highlights two non-simultaneous banana-like tracks at similar hardness but different intensities and a harder, lower intensity island-like region, indicating atoll source behavior and long term accretion variability.

and an exposure of 9.16 ks. All spectral models for the *NICER* observations include a `gaussian` component unless otherwise stated (see Table 2). Conventionally, spectra of LMXBs require at least two spectral components: a soft thermal component and a hard power-law-like non-thermal component (Remillard and McClintock, 2006; Done et al., 2007). We start by modeling the spectra with an absorbed power-law component (`tbabs*(gaussian + powerlaw)`), which yields a χ^2 value of 476.92 with 125 degrees of freedom (dof). For modeling the absorption, the abundances are taken from Wilms et al. (2000) and the cross-sections from Verner et al. (1996). To employ a more physical model for the high-energy continuum, we replace the simple power-law component with a thermal Comptonization model (`nthcomp`; Zdziarski et al. 1996; Życki et al. 1999) which gives a χ^2 value of 243.42 with 124 dof. We next test the spectra with the addition of a blackbody component with the seed photon tied to the blackbody temperature, (`tbabs*(gaussian + bbodyrad + nthcomp)`) which yields the best fit, with $\chi^2 = 111.24$ for 122 dof. Considering that the typical blackbody emission from the source is observed at a temperature of $\gtrsim 1$ keV (in't Zand et al., 2008) and the typical low-energy rollover in the spectrum is < 1 keV, we test such temperatures for the spectral fitting.

Introducing a multi-temperature disk component (`diskbb`) alongside the Comptonized continuum does not improve the fit ($\chi^2 = 133.37$ for 122 dof), and an F-test comparison between models with and without the `diskbb` component further confirms that a disk contribution is not statistically required. Thus, the *NICER* spectra favor the *Western* configuration (see Section 1), with the soft thermal component arising from the NS surface or boundary layer rather than an optically thick disk. For several *NICER* observations, the electron temperature is poorly constrained; in these cases, we fix it at 2.39 keV, the value reported by in't Zand et al. (2008). We plot the unfolded spectral decomposition of the *NICER* data and the residuals in panels (c),(e), (f) and (g) of Figure 4. Table 2 lists the best-fit parameters obtained with the model `tbabs*(gaussian+bbodyrad+nthcomp)`, with the electron temperature treated as either free or fixed at 2.39 keV. The evolution of these spectral parameters, which is a major focus of this study, is illustrated in Figure 5.

Guided by the *NICER* results, we then model the *AstroSat* spectrum using the same physical framework. To account for calibration differences between SXT and LAXPC, we apply an energy-independent scaling factor (`constant`). Fitting the spectrum with an absorbed power-law model

(`tbabs*powerlaw`) results in a statistically unacceptable fit ($\chi^2 = 418.1$ for 134 dof). Replacing the `powerlaw` with `nthcomp` yields a significant improvement ($\chi^2=248.93$ for 132 dof). Since the *AstroSat* spectra show no evidence of a high-energy rollover within the observed 0.4–20 keV band, the electron temperature (kT_e) is unconstrained. We therefore fix kT_e at 100 keV, which renders the Comptonized continuum effectively power-law-like over the *AstroSat* bandpass; under this assumption, the resulting photon index characterizes the local spectral slope rather than uniquely diagnosing the accretion state. Adding a single-temperature blackbody (`bbodyrad`) substantially improves it to a $\chi^2 = 139.04$ for 131 dof. Consistent with the *NICER* observations, adding a multicolor disk component does not improve the fit significantly ($\chi^2 = 123.17$ with 129 dof) and is disfavored by the F-test, again supporting a Western type of spectral geometry (see Section 1). Thus, we confirm that a single blackbody component adequately describes the soft spectral emission. Hence, our best-fit model for the *AstroSat* spectrum can be represented as `constant*tbabs*(bbodyrad+nthcomp)`, with the corresponding best-fit parameters listed in Table 2. Panel (c) of Figure 4 displays the unfolded SXT-LAXPC spectral model, while panel (b) shows the associated residuals. To ensure a consistent state classification across observations, we base the spectral-state identification on the relative flux contributions of the Comptonized and thermal components in the 0.5–10 keV band of *NICER* and 0.4–20 keV band of *AstroSat* (see Table 2), rather than solely on the photon index Γ . We define the Comptonized-to-blackbody flux ratio as $R = F_{\text{nthcomp}}/F_{\text{bb}}$. Following the atoll-source framework (Hasinger and van der Klis, 1989; Lin et al., 2007), we classify observations with $R \leq 6$, corresponding to spectra in which the thermal component contributes significantly or dominates, as the soft state (SS; banana branch). Observations with $R > 6$, indicative of a Comptonization-dominated spectrum, are identified as the hard state (HS; island branch). This quantitative criterion provides a uniform and reproducible demarcation between the two spectral regimes adopted in this work.

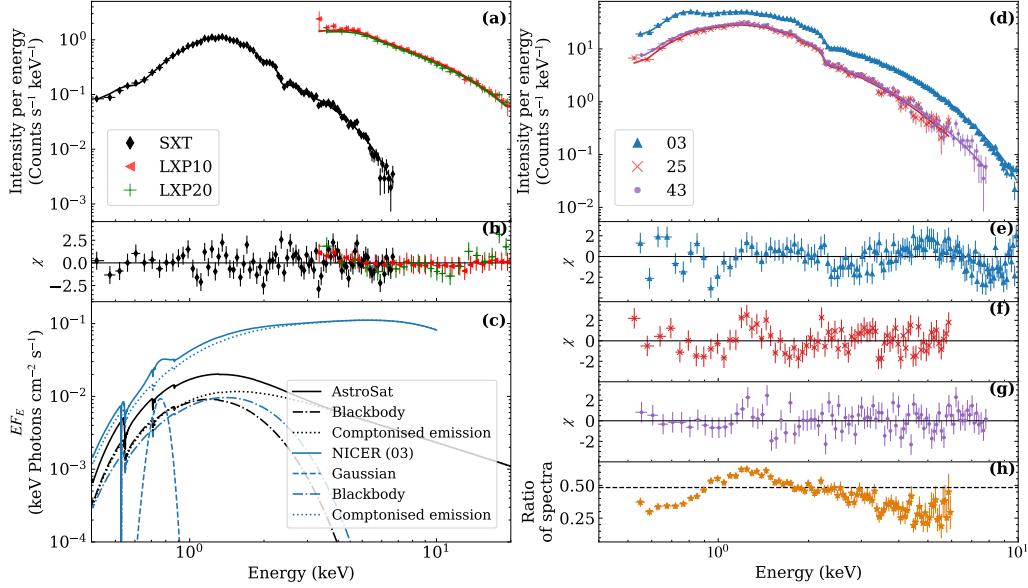


Figure 4: Broadband spectral modeling of 1A 1246–588 (see Section 3.2). (a) *AstroSat* SXT+LAXPC count spectra: black diamonds (SXT, 0.4–7 keV), red left-pointing triangles (LXP10, 3–20 keV), and green plus signs (LXP20, 3–20 keV). (b) Residuals ($\chi \equiv \text{data} - \text{model} / \text{error}$) for SXT+LAXPC using `tbabs*(bbodyrad+nthcomp)`. (c) Unfolded spectral decomposition for *AstroSat* and *NICER* with the `bbodyrad` and `nthcomp` components overplotted. (d) *NICER* count spectra (0.5–10 keV); blue upward triangles, red crosses, and purple dots correspond to ObsIDs 22009701XX (the legend lists the last two digits XX). (e)–(g) Residuals (χ) for the *NICER* spectra in panel (d) using `tbabs*(gaussian+bbodyrad+nthcomp)`; the `gaussian` component accounts for the ~ 0.75 keV instrumental feature. (h) Ratio of *NICER* spectrum #25 to #03 illustrating spectral pivoting. Together, these panels show that both *AstroSat* and *NICER* spectra are well fit with a blackbody plus thermal Comptonization without requiring an additional disk component, and reveal state-dependent spectral changes across the *AstroSat* and *NICER* observations.

Table 2: Best-fit spectral parameters for 1A 1246–588 from *AstroSat* (SXT+LAXPC) and *NICER* (see Section 3.2), using the model **tbabs*(gaussian+bbbodyrad+nthcomp)** with the Comptonizing electron temperature left free unless noted. Units are indicated in the column headers. Errors are 1σ . This table summarizes the spectral decomposition across epochs and enables comparison of the thermal and Comptonized contributions to the observed flux.

Obs. ID (State)*	tbabs	gaussian [†]	bbbodyrad			nthcomp				χ^2/dof
	N_{H} ($\times 10^{21} \text{ cm}^{-2}$)	norm ($\times 10^{-3}$)	kT_{bb} (keV)	norm ^a ($\times 10^2$)	Flux ^c ($\times 10^{-11}$) ^b	Γ	kT_{e} (keV)	norm ($\times 10^{-2}$)	Flux ^c ($\times 10^{-11}$) ^b	
–	$2.59^{+0.17}_{-0.18}$	–	0.33 ± 0.01	$2.47^{+0.29}_{-0.24}$	3.16 ± 0.11	2.05 ± 0.02	100 [‡]	$1.37^{+0.09}_{-0.08}$	11.9 ± 0.2	139.04/131
					<i>AstroSat</i> ^d					
					<i>NICER</i>					
01 (SS)	1.56 ± 0.07	0.86 ± 0.09	0.37 ± 0.01	1.74 ± 0.09	2.25 ± 0.07	1.95 ± 0.04	2.39^e	$1.62^{+0.14}_{-0.13}$	13.5 ± 0.3	151.14/111
02 (SS)	$1.46^{+0.07}_{-0.06}$	3.13 ± 0.14	0.37 ± 0.01	$3.12^{+0.23}_{-0.24}$	$5.62^{+0.09}_{-0.10}$	$1.63^{+0.05}_{-0.06}$	$1.88^{+0.12}_{-0.10}$	$2.91^{+0.36}_{-0.34}$	30.2 ± 0.8	90.49/120
03 (SS)	1.44 ± 0.05	3.45 ± 0.13	0.38 ± 0.01	3.53 ± 0.16	$7.74^{+0.08}_{-0.09}$	$1.50^{+0.05}_{-0.04}$	$1.66^{+0.06}_{-0.05}$	$2.41^{+0.30}_{-0.25}$	$30.5^{+0.8}_{-0.9}$	112.35/123
04 (HS)	$0.91^{+0.10}_{-0.09}$	1.47 ± 0.08	0.37 ± 0.02	$0.73^{+0.27}_{-0.38}$	$1.31^{+0.07}_{-0.06}$	$2.00^{+0.10}_{-0.11}$	$2.4^{+0.8}_{-0.4}$	$1.99^{+0.36}_{-0.31}$	14.5 ± 0.2	100.66/104
05 (HS)	$1.08^{+0.12}_{-0.11}$	1.02 ± 0.10	0.38 ± 0.02	$1.00^{+0.14}_{-0.20}$	$0.92^{+0.09}_{-0.05}$	2.01 ± 0.07	2.39^e	$1.66^{+0.29}_{-0.24}$	$13.9^{+0.2}_{-0.3}$	85.40/89
06 (SS)	1.88 ± 0.08	$0.06^{+0.08}_{-0.06}$	0.37 ± 0.01	1.54 ± 0.09	$2.55^{+0.06}_{-0.07}$	1.97 ± 0.05	2.39^e	$1.32^{+0.14}_{-0.13}$	10.4 ± 0.4	124.84/92
07 (SS)	1.79 ± 0.08	0.08 ± 0.08	0.39 ± 0.01	1.64 ± 0.07	2.94 ± 0.06	1.83 ± 0.05	2.39^e	$1.00^{+0.11}_{-0.10}$	$10.0^{+0.3}_{-0.2}$	121.55/101
08 (SS)	2.1 ± 0.1	N	0.38 ± 0.01	$2.0^{+0.1}_{-0.2}$	$4.07^{+0.06}_{-0.05}$	$1.70^{+0.20}_{-0.10}$	$1.7^{+0.5}_{-0.2}$	$0.85^{+0.29}_{-0.14}$	$7.9^{+0.6}_{-0.5}$	84.60/91
22 (HS)	$3.77^{+0.25}_{-0.23}$	N	0.29 ± 0.02	$3.03^{+0.53}_{-0.48}$	$1.46^{+0.20}_{-0.18}$	$2.18^{+0.07}_{-0.08}$	2.39^e	$2.02^{+0.37}_{-0.31}$	$10.8^{+0.7}_{-0.8}$	109.78/78
23 (SS)	$3.75^{+0.18}_{-0.13}$	N	$0.30^{+0.01}_{-0.02}$	$3.23^{+0.41}_{-0.62}$	2.47 ± 0.10	$2.09^{+0.22}_{-0.14}$	$1.9^{+1.6}_{-0.4}$	$1.70^{+0.46}_{-0.28}$	$8.9^{+0.7}_{-0.7}$	116.77/88
24 (SS)	4.0 ± 0.2	N	0.28 ± 0.02	$2.58^{+0.51}_{-0.66}$	3.79 ± 0.11	$2.30^{+0.08}_{-0.09}$	2.39^e	$2.17^{+0.40}_{-0.34}$	$6.5^{+0.8}_{-0.5}$	108.74/65
25 (SS)	$3.31^{+0.26}_{-0.23}$	N	$0.31^{+0.02}_{-0.03}$	$2.27^{+0.47}_{-0.63}$	2.20 ± 0.18	$2.22^{+0.13}_{-0.15}$	2.39^e	$1.81^{+0.52}_{-0.41}$	9.2 ± 1.0	93.78/71
26 (HS)	3.9 ± 0.3	N	0.28 ± 0.02	$2.6^{+0.5}_{-0.4}$	$0.84^{+0.16}_{-0.07}$	2.22 ± 0.09	2.39^e	$1.53^{+0.36}_{-0.28}$	$8.3^{+0.4}_{-0.6}$	82.94/87
28 (SS)	$2.71^{+0.12}_{-0.11}$	N	$0.33^{+0.01}_{-0.02}$	$2.29^{+0.06}_{-0.68}$	$2.77^{+0.07}_{-0.08}$	$1.95^{+0.38}_{-0.05}$	$1.6^{+9.8}_{-0.4}$	$1.3^{+0.5}_{-0.1}$	$8.2^{+0.6}_{-0.3}$	103.66/76
30 (SS)	1.83 ± 0.09	0.28 ± 0.07	0.36 ± 0.01	$1.28^{+0.13}_{-0.15}$	$5.31^{+0.03}_{-0.02}$	2.07 ± 0.06	2.39^e	$1.47^{+0.18}_{-0.16}$	5.6 ± 0.1	114.82/77
31 (SS)	$1.12^{+0.08}_{-0.07}$	0.76 ± 0.07	0.36 ± 0.01	0.9 ± 0.1	$2.11^{+0.05}_{-0.07}$	2.00 ± 0.06	2.39^e	$2.12^{+0.25}_{-0.21}$	11.4 ± 0.3	87.84/87
32 (HS)	$1.52^{+0.09}_{-0.08}$	1.73 ± 0.10	0.36 ± 0.01	$1.09^{+0.13}_{-0.12}$	0.91 ± 0.09	2.03 ± 0.06	2.39^e	$1.84^{+0.23}_{-0.20}$	16.1 ± 0.3	82.02/97
33 (SS)	1.30 ± 0.03	2.80 ± 0.13	0.35 ± 0.01	3.41 ± 0.04	5.17 ± 0.04	1.50 ± 0.01	$1.33^{+0.01}_{-0.12}$	1.69 ± 0.01	17.1 ± 0.1	109.34/88
34 (SS)	$1.19^{+0.09}_{-0.08}$	2.49 ± 0.12	0.35 ± 0.01	$2.44^{+0.28}_{-0.33}$	$3.53^{+0.09}_{-0.08}$	$1.74^{+0.08}_{-0.09}$	$1.87^{+0.21}_{-0.17}$	$2.35^{+0.38}_{-0.36}$	$19.9^{+0.6}_{-0.7}$	126.56/108

Continued on next page

Table 2 (continued)

36 (SS)	1.4 ± 0.1	0.4 ± 0.1	0.38 ± 0.01	$1.47^{+0.11}_{-0.12}$	$2.65^{+0.09}_{-0.08}$	1.85 ± 0.08	2.39^e	1.2 ± 0.2	$10.8^{+0.5}_{-0.6}$	104.02/84
37 (SS)	2.1 ± 0.1	N	0.36 ± 0.01	1.91 ± 0.12	$2.68^{+0.08}_{-0.07}$	1.92 ± 0.05	2.39^e	$1.30^{+0.14}_{-0.13}$	10.3 ± 0.5	120.81/102
38 (SS)	1.54 ± 0.09	0.37 ± 0.08	0.38 ± 0.01	$1.28^{+0.12}_{-0.14}$	$5.96^{+0.03}_{-0.04}$	2.03 ± 0.08	2.39^e	1.3 ± 0.2	5.4 ± 0.1	101.34/78
39 (SS)	$1.97^{+0.12}_{-0.11}$	0.31 ± 0.12	0.38 ± 0.01	$1.75^{+0.13}_{-0.12}$	2.85 ± 0.09	1.86 ± 0.07	2.39^e	$1.08^{+0.17}_{-0.15}$	$10.1^{+0.5}_{-0.6}$	105.98/97
40 (SS)	1.74 ± 0.03	0.41 ± 0.07	0.38 ± 0.01	$1.72^{+0.02}_{-0.28}$	$3.62^{+0.03}_{-0.02}$	$1.72^{+0.13}_{-0.01}$	$1.58^{+0.49}_{-0.24}$	$0.95^{+0.24}_{-0.01}$	8.3 ± 0.1	114.85/91
41 (SS)	1.96 ± 0.09	0.16 ± 0.08	0.37 ± 0.01	1.58 ± 0.11	$2.80^{+0.07}_{-0.06}$	1.98 ± 0.06	2.39^e	$1.27^{+0.16}_{-0.15}$	9.3 ± 0.4	120.12/89
42 (SS)	$3.35^{+0.20}_{-0.18}$	N	0.31 ± 0.02	$1.81^{+0.42}_{-0.60}$	$4.47^{+0.11}_{-0.10}$	$2.38^{+0.08}_{-0.09}$	2.39^e	$2.10^{+0.40}_{-0.33}$	$5.9^{+0.2}_{-0.6}$	88.57/72
43 (SS)	$2.72^{+0.18}_{-0.17}$	N	0.35 ± 0.02	$2.24^{+0.24}_{-0.23}$	2.46 ± 0.13	2.03 ± 0.10	2.39^e	$1.35^{+0.28}_{-0.24}$	$9.8^{+0.7}_{-0.8}$	95.39/87

* HS = hard state, SS = soft state.

† Line energy and width for the Gaussian component are frozen at 0.75 keV and 0.05 keV, respectively.

‡ Parameter frozen.

^a **bbodyrad** normalization: $\text{norm} = (R_{\text{bb}}/D_{10})^2$, where R_{bb} is the apparent emitting radius (km) and D_{10} is distance in units of 10 kpc. The apparent radius inferred from the **bbodyrad** normalization does not include spectral hardening or gravitational redshift effects, and the physical emitting radius can be estimated as $R \simeq f_c^2 R_{\text{bb}}/(1+z)$, where f_c is the color-correction factor and z is the gravitational redshift.

^b Unabsorbed flux in $\text{erg cm}^{-2} \text{s}^{-1}$ estimated with **cflux** on the corresponding component.

^c Flux is over 0.5–10 keV for *NICER* and 0.4–20 keV for *AstroSat*.

^d Gain offset = 45 ± 3 eV; cross-normalization constants $C_{\text{LXP10}} = 0.85 \pm 0.03$, $C_{\text{LXP20}} = 0.88 \pm 0.02$; $C_{\text{SXT}} = 1$ (fixed).

^e indicates the parameter was fixed at that value.

N: not detected.

4. Results and Discussion

We investigate the variability of the UCXB 1A 1246–588 by combining long-term *MAXI*/GSC monitoring with pointed *NICER* and *AstroSat* observations. The *MAXI* light curve reveals long-term flux variations that contextualize the shorter timescale variability observed with *NICER*. Broadband spectral modeling of the *NICER* and *AstroSat* data corroborates earlier results (in’t Zand et al., 2008) and enables a systematic study of changes in the relative contributions of thermal and Comptonized emission across luminosity states. The *AstroSat* observation, obtained during a low-intensity phase, further probes the source at harder energies (0.4–20 keV), offering additional constraints on the thermal and Comptonized components. Together, these observations present the first coherent view of the spectral evolution of 1A 1246–588 across distinct luminosity states, highlighting its variable accretion behavior.

4.1. Light curve properties using *NICER* and *MAXI*

We characterize the X-ray variability of 1A 1246–588 on day timescales using pointed *NICER* observations and long-term monitoring data from *MAXI*. The *NICER* observations (Figure 1) samples the source densely over ~ 75 days and shows pronounced intensity variations, including distinct rises in the 3–10 keV intensity. These variations are accompanied by correlated changes in hardness (see Section 3.1), indicating that the observed variability arises from spectral-state transitions, likely driven by fluctuations in the accretion rate, which govern the changing balance between the thermal and Comptonized emission components (Done et al., 2007). On longer timescales, in’t Zand et al. (2008) reported variability ranging from weeks to hundreds of days based on ASM/PCA/BAT monitoring, highlighting a persistently active source. To place the *NICER* coverage in this broader context, we depict the *MAXI* 1-day light curve spanning several months around the *NICER* and *AstroSat* epochs. Over these baselines, the *MAXI* light curve traces the long-term flux evolution and confirms that the *NICER* observation occurred during an active phase. For the *AstroSat* epoch, *MAXI* coverage is sparse, and the surrounding flux measurements are low, consistent with the soft, low-intensity state we identify in our spectral analysis. The epochs of the *NICER* and *AstroSat* observations fall within activity levels consistent with the high and low-flux states reported by in’t Zand et al. (2008). Based on long-term *MAXI* monitoring, Asai et al. (2022) classified 1A 1246–588

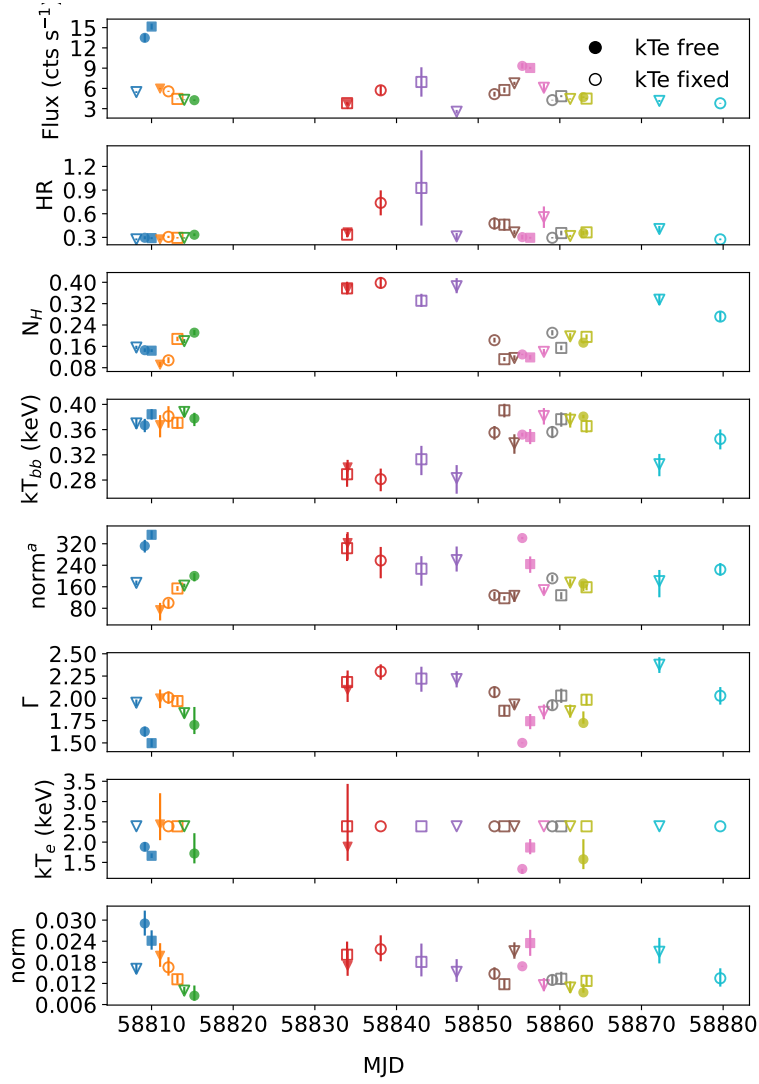


Figure 5: Temporal evolution of the best-fit spectral parameters obtained from *NICER* (see Section 3.2) using the best-fit model `tbabs*(gaussian+bbodyrad+nthcomp)`. Panels from top to bottom show: the 3–10 keV background-subtracted intensity; the hardness ratio (5–10 keV / 3–5 keV); the hydrogen column density N_{H} ; the blackbody temperature kT_{bb} ; the `bbodyrad` normalization (reported as $(R/D_{10})^2$); the Comptonization photon index Γ ; the electron temperature kT_e ; and the `nthcomp` normalization. Each point corresponds to an individual *NICER* observation (ObsID 22009701XX; see Figure 1), color-coded consistently across panels. The hollow symbols indicate observations for which the electron temperature was fixed at $kT_e = 2.39$ keV. All of the values are as listed in Table 2. A narrow `gaussian` emission component at ~ 0.75 keV is included when required but is not shown. The evolution reveals clear spectral changes, including correlated variations between the thermal and Comptonized components, indicative of state-dependent spectral evolution.

as a modified periodic (MP) source exhibiting quasi-periodic variations on $\sim 2.5\text{--}10$ yr timescales. In the Asai et al. (2022) light curve, the epoch corresponding to our *AstroSat* observation lies in a relatively low-flux interval, whereas the *NICER* campaign overlaps a brighter phase of the long-term modulation. This matches our MAXI snapshots, which show low daily rates around the *AstroSat* window and significantly elevated activity during the *NICER* window. This indicates that 1A 1246–588 exhibits multi-timescale variability: short-term flux changes captured by the pointed observations are superposed on longer-term luminosity modulations reported in previous studies (Barret et al., 2000; Asai et al., 2022). Finally, the *NICER* campaign (0.2–12 keV) reinforces the picture established by in’t Zand et al. (2008) of 1A 1246–588 as a persistently active source exhibiting moderate, short-term flux variability. These variations likely arise from short-term spectral-state changes driven by fluctuations in the accretion flow, reflecting evolving accretion and Comptonization conditions (see Sections 3.1 and 3.2).

4.2. HID properties using *NICER* and *AstroSat*

The HID (Figure 3) provides a clear view of the source’s spectral-state behavior across the *NICER* and *AstroSat* observations. The *AstroSat* epoch (black point; Figure 3) occupies a region of relatively low intensity and high hardness. This comparatively harder location of the *AstroSat* point in the HID arises from the adopted hardness definition (5–10 keV / 3–5 keV), which probes energy bands where the Comptonized component dominates even in the soft state. Consequently, the hardness ratio appears elevated relative to *NICER*-based HIDs that include softer energy bands more sensitive to the thermal emission. $R = F_{\text{nthcomp}}/F_{\text{bb}} \approx 3.8$. According to our adopted flux-ratio criterion ($R \leq 6$ for the soft state), this places the source in the soft state. Although the *AstroSat* point appears on the harder side of the HID, this location reflects the chosen hardness definition (5–10 keV / 3–5 keV), which emphasizes the Comptonized emission. The flux decomposition confirms that the thermal component still contributes substantially to the total emission (see Table 2).

Within the *NICER* data the HID reveals a horizontal track (blue points; Figure 3) resembling the “banana” branch commonly observed in atoll sources (e.g., Hasinger and van der Klis, 1989; van der Klis, 2004). At a later epoch, the source traces a second set of points (pink; Figure 3) at lower intensity, representing the early phase of a transition toward the softer banana branch. These two excursions of a banana-like track, while slightly varying in peak

flux, share comparable hardness and position on the HID. This suggests that the source reached similar spectral states across distinct epochs, likely reflecting moderate long-term variations in the accretion rate. Additionally, between the epochs tracing the higher-intensity banana track (blue points; Figure 3) and those characterized by low intensity and low hardness, some observations extend toward higher hardness at similarly low intensities. Among these, ObsID 2200970125 (purple; Figure 3) occupies a region of low intensity and high hardness, consistent with island-state morphology (Hasinger and van der Klis, 1989; Gierliński and Done, 2002). These HID patterns are consistent with the classifications observed in other atoll sources (e.g., Church et al., 2014). This state is generally associated with lower accretion rates and enhanced Comptonization, in contrast to the banana branch, where thermal emission dominates. In the context of state transitions, the pink points likely represent the progression of the Comptonization dominated island state towards the thermally dominated banana branch, with the spectrum softening as the thermal component becomes more prominent.

Overall, the HID demonstrates that 1A 1246–588 samples multiple spectral states, with the banana branch showing short-term spectral state changes reflecting evolving accretion and Comptonization, and the island state representing a harder, low-luminosity regime. In this context, spectral state identification is based on hardness and relative component fluxes rather than on the photon index alone, which can be model-dependent when the Comptonizing electron temperature is fixed or unconstrained (Lin et al., 2007). These spectral-state mappings, when combined with the temporal information from the light curves (Section 4.1), provide a comprehensive view of the source’s accretion behavior and state transitions.

4.3. Evolution of the spectral properties of 1A 1246–588

Motivated by the source’s evolution along the HID, we investigate its spectral properties during the persistent state to assess how they vary across different spectral states. The observed broadband flux of 1A 1246–588 in 0.5–10 keV of *NICER* data (see Figure 1) is between 0.7×10^{-10} and 3.7×10^{-10} erg cm⁻² s⁻¹. The epochs analyzed here are at flux levels comparable to the PCA low-flux state reported by in’t Zand et al. (2008). The source exhibits a broadband spectrum that requires multiple components to be adequately modeled. The dominant emission components in the 0.5–10 keV *NICER* band, and the 0.4–7 keV *AstroSat*-SXT and 3–20 keV *AstroSat*-LAXPC band are shown in Figure 4. Another aspect to emphasize

is *AstroSat*'s broader energy coverage compared to *NICER*, which enables tighter constraints on spectral components (Singh et al., 2016; Armas Padilla, M. et al., 2023).

5. Spectral Evolution and Accretion States

Our spectral analysis reveals that the absorption column density to sufficiently model the soft X-ray spectra of 1A 1246–588 lies within $1 \times 10^{21} \text{ cm}^{-2}$ to $4 \times 10^{21} \text{ cm}^{-2}$ for *NICER* observations. This is broadly consistent with the line of sight column density as measured from the HI maps ($3.35 \times 10^{21} \text{ cm}^{-2}$; HI4PI Collaboration et al., 2016) and also consistent with the archival observations (in't Zand et al., 2008). However, the relatively wide spread in fitted N_{H} values across individual *NICER* spectra, which is larger than typically expected for ultra-compact systems, does not necessarily imply genuine variability in the absorbing material and may instead reflect degeneracies between N_{H} and other spectral components in the modeling. The analysis of the *AstroSat* observations also require a $N_{\text{H}} = 2.6 \times 10^{21} \text{ cm}^{-2}$ which is consistent with the previous estimates. Overall, the fitted column densities are consistent with previous measurements, and the available data do not provide clear evidence for long-term changes in the absorption toward the source.

Typically in NS UCXBs, the thermal emission is modeled as originating either from the NS boundary layer or from the accretion disk. In the present analysis, where the thermal component is represented solely by a blackbody, the inferred blackbody temperature spans 0.28–0.39 keV. The blackbody normalization (see Table 2 for definition) lies in the range 100–400, corresponding to an apparent emitting radius of $R_{\text{bb}} \simeq 4.3\text{--}8.6 \text{ km}$. This represents the apparent radius derived from the `bodyrad` model and does not include spectral hardening effects. Applying a representative color-correction factor $f_{\text{c}} \simeq 1.6$, appropriate for neutron-star surface or boundary-layer emission (e.g., Suleimanov et al., 2012), and neglecting gravitational redshift for simplicity, the inferred physical radius increases to $R \simeq 6.9\text{--}13.8 \text{ km}$. These values remain consistent with emission from an extended region at the disk–NS interface, such as a boundary layer, rather than from a localized hot spot on the stellar surface alone (Inogamov and Sunyaev, 1999; Lin et al., 2007). The inclusion of an additional multicolor disk blackbody component does not result in a statistically significant improvement in the fits, as confirmed by the F-test. Given the ultra-compact nature of the system and its short

orbital period, the accretion disk is expected to be physically small (e.g., Frank et al. 2002; van Haaften, L. M. et al. 2012). In such a configuration, any emission from a cool, compact disk would be intrinsically weak and readily outshone by the Comptonized component fed by seed photons from the NS surface. The absence of a detectable disk blackbody contribution in our fits is therefore consistent with Comptonization occurring in an extended accretion-disk corona, as described in the Birmingham (Western) model geometry for LMXBs, where the spectrum is dominated by a soft blackbody boundary layer and a hard Comptonized component (Church and Bałucińska-Church, 2004). The low-flux spectrum of 1A 1246–588 from *RXTE*/*PCA* in in’t Zand et al. (2008) indicates that the spectrum has to be modeled with a power-law. in’t Zand et al. (2008) also find that this power-law is better described by a Comptonized emission, which in our analysis is `nthcomp`. For several *NICER* observations, the electron temperature could not be independently constrained due to the limited energy coverage. In these cases, we fixed the electron temperature at $kT_e = 2.39$ keV, adopting the value reported for the high-flux Comptonized component in the *Swift-XRT+PCA* analysis of in’t Zand et al. (2008). Fixing kT_e stabilizes the fits and allows the photon index (Γ) to be constrained; under this assumption, small variations in Γ likely reflect parameter degeneracy rather than intrinsic changes in the Comptonizing plasma. In the *NICER* observations, although the 0.5–10 keV flux is often dominated by the Comptonized component, the fitted spectral parameters (Γ and kT_e), together with the inferred optical depth (τ), indicate a soft, optically thick Comptonization regime (Zdziarski et al., 1996; Done et al., 2007)(see Table 2). In the *AstroSat* observation, no high-energy cutoff is detected; therefore, the Comptonized component is constrained by the photon index, and the electron temperature is fixed at $kT_e = 100$ keV to approximate a power-law spectrum over the observed bandpass (Shidatsu et al., 2017). The resulting photon index, $\Gamma \simeq 2.05$, characterizes the spectral slope under this assumption. While this value lies within the range of photon indices measured during the softer, banana-like states in the *NICER* campaign, the *NICER* spectra require a much lower electron temperature ($kT_e \simeq 2\text{--}3$ keV), implying a physically distinct Comptonizing plasma. Because Γ in the `nthcomp` model depends explicitly on kT_e , the Comptonization parameters derived from the *AstroSat* and *NICER* spectra are not directly comparable, and similarities in Γ do not imply comparable coronal properties. The apparent differences in electron temperature are therefore most naturally attributed to the differing energy coverage and in-

strumental responses of *AstroSat* and *NICER*, which are known to introduce systematic differences in inferred Comptonization parameters (Kolehmainen et al., 2013; Madsen et al., 2017). In addition, the source occupies different regions of the hardness–intensity diagram during the *AstroSat* and *NICER* epochs, and the Comptonization parameters, particularly the electron temperature; differ markedly, together suggesting that the source was observed in different spectral states, consistent with the long-term flux differences shown in Figure 2. As noted above, the photon index Γ is not used as a primary spectral-state diagnostic in this work, because its inferred value depends sensitively on the assumed electron temperature and on the limited energy coverage of the instruments, particularly for *NICER*. Instead, spectral states are identified using the HID and the relative flux contributions of the Comptonized and thermal components, which provide a more robust and physically meaningful classification across both epochs.

Building on these considerations, we examine the evolution of the Comptonized component in relation to the thermal emission using the `nthcomp` model. Across the *NICER* observations, we find a clear inverse relationship between the photon index (Γ) and the blackbody temperature (Figure 5). Over the observed range of blackbody temperatures ($kT_{\text{bb}} \simeq 0.27\text{--}0.39$ keV), the characteristic energy of the seed photons increases correspondingly, shifting the low-energy rollover of the Comptonized spectrum toward higher energies (Done et al., 2007). Over the observed blackbody temperature range, the photon index spans $\Gamma \simeq 1.5\text{--}2.4$, with harder spectra generally associated with higher blackbody temperatures, indicating a broad anti-correlation between kT_{bb} and Γ . Restricting the analysis to observations in which the electron temperature is free, a Spearman rank correlation test yields $r_s = -0.6$ with a p-value of 8.8×10^{-2} ($n = 9$). While the inferred trend is consistent with an anti-correlation, its statistical significance is marginal given the limited sample size. This behavior is consistent with the source transitioning between island-like and banana-like accretion states. Harder spectra, with photon indices $\Gamma \sim 1.5$, are typically associated with island states characterized by reduced seed photon input and a relatively stronger Comptonized contribution, whereas softer spectra ($\Gamma \sim 2.4$) correspond to banana states with higher accretion rates and enhanced thermal emission from the disk or boundary layer (Barret et al., 2000; Armas Padilla et al., 2017; Zdziarski et al., 1996). However, the substantial scatter in Γ , particularly in observations where the electron temperature is fixed at 2.39 keV, suggests that part of this trend is influenced by parameter coupling in the spectral modeling

rather than reflecting purely intrinsic changes in the Comptonizing plasma.

Using the photon indices and electron plasma temperature, the optical depth of the Comptonizing cloud (τ) can be estimated following Sunyaev and Titarchuk (1980):

$$\Gamma = -\frac{1}{2} + \sqrt{\frac{9}{4} + \gamma}, \quad \text{where} \quad \gamma = \pi^3 \frac{kT_e}{m_e c^2} \left(\tau^2 + \frac{2}{3} \right)$$

. This yields optical depths in the range $\tau \simeq 3.3\text{--}6.7$, consistent with a soft or banana-state Comptonization regime (Gierliński and Done, 2002; Done et al., 2007). We note that these values depend on the assumed electron temperature; with the current data, the degeneracy between kT_e and τ cannot be resolved. In the subset of nine observations where kT_e is left free, the electron temperature spans $kT_e \simeq 1.34\text{--}2.44$ keV. While these variations broadly coincide with changes in source hardness and intensity, the limited high-energy sensitivity of the data prevents a systematic assessment of kT_e across all observations.

To investigate the origin of the spectral evolution, Figure 6 illustrates how the relative contributions of the Comptonized and thermal components govern the *NICER* spectra. In the left panel of Figure 6, we plot the ratio of the Comptonized flux to the blackbody flux as a function of the total 0.5–10 keV flux. At lower total fluxes, corresponding to island states, the flux ratio is high, indicating that the Comptonized component dominates the emission. As the source brightens, this ratio decreases systematically, reflecting the growing contribution of the blackbody component. This behavior qualitatively reproduces the hardness–intensity evolution seen in the HID (Figure 3), demonstrating that changes in spectral hardness arise from variations in the relative strengths of the Comptonized and thermal components. The right panel of Figure 6 shows the evolution of the individual component fluxes with total flux. The Comptonized and blackbody fluxes exhibit a clear anti-correlation, with the emission at lower luminosities dominated by the Comptonized component, corresponding to island-like behavior. Above this range, the increasing blackbody flux reflects a growing thermal contribution to the total emission. For the *AstroSat* observation, the Comptonized-to-blackbody flux ratio in the 0.4–20 keV band is $R \approx 3.8$ (see Table 2), placing it within the soft-state regime under our adopted criterion. This indicates that, despite a significant Comptonized contribution, the thermal component remains energetically important. In the context of accretion geometry,

such spectra are consistent with configurations in which the optically thick inner accretion flow contributes prominently, while Comptonization remains active but does not dominate the energy budget. A direct illustration of the state-dependent spectral changes in the *NICER* observations is provided by the comparison between ObsID 200970103 and ObsID 200970125, shown in panel (h) of Figure 4. ObsID 03, which lies on the banana branch of the HID, exhibits a softer spectrum characterized by a higher blackbody temperature ($kT_{\text{bb}} \simeq 0.38$ keV), a larger blackbody normalization (corresponding to a larger emitting area), indicative of enhanced thermal emission from the NS boundary layer and a relatively weaker Comptonized contribution. In contrast, ObsID 25, associated with the island state, shows a harder spectrum with a lower blackbody temperature ($kT_{\text{bb}} \simeq 0.31$ keV), and reduced blackbody flux, reflecting a diminished thermal component and a comparatively stronger role of Comptonization (Table 2). This ratio spectrum clearly demonstrates spectral pivoting, with the island-state spectrum becoming harder at higher energies while being relatively suppressed at soft energies, in agreement with the flux–ratio trends. While such behavior is qualitatively consistent with changes in the balance between the thermal and Comptonized emission components as the source transitions between the banana and island states, we note that significant degeneracy exists between N_{H} , the soft thermal component (kT_{bb}), and the Comptonized continuum. Consequently, the relative flux contributions of individual components are not uniquely constrained. The observed spectral evolution therefore likely reflects changes in the overall spectral shape, which may arise from variations in the relative strengths of the thermal and Comptonized emission, as expected for atoll-type NS systems (Hasinger and van der Klis, 1989; Gierliński and Done, 2002).

6. Summary

We present a comprehensive temporal and spectral study of the ultra-compact X-ray binary 1A 1246–588 using long-term *MAXI*/GSC monitoring, and pointed observations from *NICER* and *AstroSat*. Our analysis establishes, for the first time, a coherent picture of the source’s spectral evolution across different flux states.

- Our *AstroSat* observation falls in a low-flux segment of the *MAXI* light-curve variations, while the *NICER* campaign coincides with a brighter

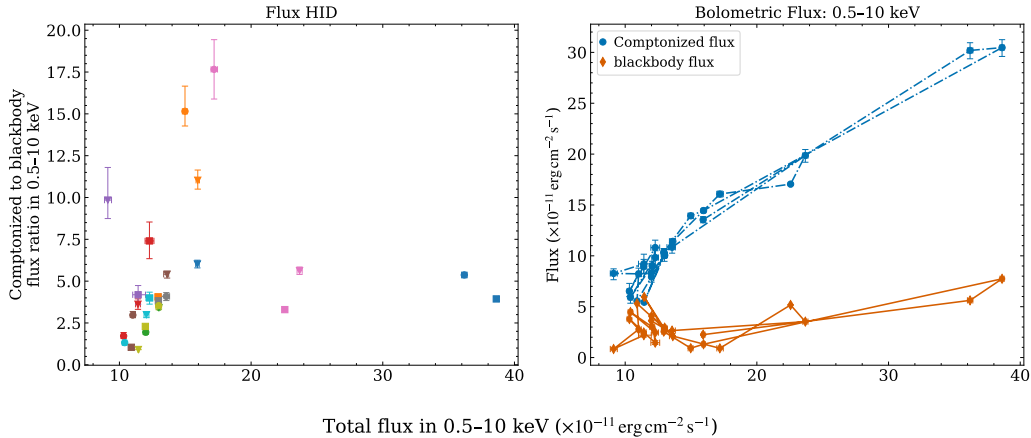


Figure 6: Flux ratios of all *NICER* observations (see section 5). Left Panel: Ratio of the Comptonized flux to blackbody flux as a function of the total flux in 0.5–10 keV. The color and symbols of the observations are kept identical to Figure 1. This panel demonstrates consistency with the HID. Right Panel: Evolution of the Comptonized flux and the blackbody flux as a function of the total flux in 0.5–10 keV as well. This panel highlights a clear anti-correlation between the thermal and Comptonized components across the observed flux range.

phase. Within these intervals, *NICER* data reveals strong short-term flux excursions atop a broadly stable emission level.

- The *NICER* HID shows an atoll-like pattern, with a single banana-like track, along which the source undergoes two phases of higher intensity and a cluster of hard, low-flux points marking an island state, indicating transitions between Comptonization and thermal dominance as the source evolves in luminosity.
- The emission consists of a soft blackbody component ($kT = 0.27$ – 0.39 keV, radius ~ 7 – 14 km) consistent with boundary-layer emission, plus a harder Comptonized tail that steepens from $\Gamma \approx 1.5$ – 2.4 as the source brightens.
- The spectral evolution is driven by shifts in the balance between the boundary-layer emission and the Comptonizing corona, which vary in a contrasting manner across the 0.5–10 keV flux range, with the transition from island to banana states corresponding to a softening of the spectrum as the thermal component strengthens and the Comptonized

emission weakens.

Acknowledgments

This research has made use of *NICER*'s data obtained through the High Energy Astrophysics Science Archive Research Center (HEASARC) Online Service, provided by the NASA/Goddard Space Flight Center. This work has also utilized data from the *AstroSat* mission of the Indian Space Research Organisation (ISRO), archived at the Indian Space Science Data Centre (ISSDC). The paper has used data from the SXT and the LAXPC instruments developed at the Tata Institute of Fundamental Research (TIFR), Mumbai. The *AstroSat* Payload Operation Centers at TIFR are thanked for verifying and releasing the data via the ISSDC data archive and providing the necessary software tools.

Facilities: *AstroSat*, *NICER*

Software: astropy (Astropy Collaboration et al., 2018),

Declaration of generative AI and AI-assisted technologies in the manuscript preparation process

During the preparation of this work the author(s) used ChatGPT (OpenAI) in order to assist with grammar checking and sentence refinement. After using this tool/service, the author(s) reviewed and edited the content as needed and take(s) full responsibility for the content of the published article.

References

- Antia, H.M., Agrawal, P.C., Katoch, T., Manchanda, R.K., Mukerjee, K., Shah, P., 2022. Improved Background Model for the Large Area X-Ray Proportional Counter (LAXPC) Instrument on board *AstroSat*. *Astrophys. J. Suppl. Ser.* 260, 40. doi:10.3847/1538-4365/ac6dd0, arXiv:2205.03136.
- Armas Padilla, M., Degenaar, N., Wijnands, R., 2017. X-ray spectral states of accreting neutron stars. *Mon. Not. R. Astron. Soc.* 467, 290–304. doi:10.1093/mnras/stx079.

- Armas Padilla, M., Corral-Santana, J. M., Borghese, A., Cúneo, V. A., Muñoz-Darias, T., Casares, J., Torres, M. A. P., 2023. Ultracompat: A comprehensive catalogue of ultra-compact and short orbital period x-ray binaries. *Astron. Astrophys.* 677, A186. doi:10.1051/0004-6361/202346797.
- Arzoumanian, Z., Gendreau, K.C., Baker, C.L., Cazeau, T., Hestnes, P., Kellogg, J.W., Kenyon, S.J., Kozon, R.P., Liu, K.C., Manthripragada, S.S., Markwardt, C.B., Mitchell, A.L., Mitchell, J.W., Monroe, C.A., Oka-jima, T., Pollard, S.E., Powers, D.F., Savadkin, B.J., Winternitz, L.B., Chen, P.T., Wright, M.R., Foster, R., Prigozhin, G., Remillard, R., Doty, J., 2014. The neutron star interior composition explorer (NICER): mission definition, in: Takahashi, T., den Herder, J.W.A., Bautz, M. (Eds.), *Space Telescopes and Instrumentation 2014: Ultraviolet to Gamma Ray*, p. 914420. doi:10.1117/12.2056811.
- Asai, K., Mihara, T., Matsuoka, M., 2022. Decades-long variations in NS-LMXBs observed with MAXI/GSC, RXTE/ASM, and Ginga/ASM. *Publ. Astron. Soc. Jpn.* 74, 974–990. doi:10.1093/pasj/psac049, arXiv:2206.02299.
- Astropy Collaboration, Price-Whelan, A.M., Sipőcz, B.M., Günther, H.M., Lim, P.L., Crawford, S.M., Conseil, S., Shupe, D.L., Craig, M.W., Dencheva, N., Ginsburg, A., VanderPlas, J.T., Bradley, L.D., Astropy Contributors, 2018. The Astropy Project: Building an Open-science Project and Status of the v2.0 Core Package. *Astron. J.* 156, 123. doi:10.3847/1538-3881/aabc4f, arXiv:1801.02634.
- Barret, D., Olive, J.F., Boirin, L., Done, C., Skinner, G.K., Grindlay, J.E., 2000. Hard X-Ray Emission from Low-Mass X-Ray Binaries. *Astrophys. J.* 533, 329–351. doi:10.1086/308651, arXiv:astro-ph/9911042.
- Bassa, C.G., Jonker, P.G., in't Zand, J.J.M., Verbunt, F., 2006. Two new candidate ultra-compact X-ray binaries. *Astron. Astrophys.* 446, L17–L20. doi:10.1051/0004-6361:200500229, arXiv:astro-ph/0601045.
- Bhattacharya, D., van den Heuvel, E.P.J., 1991. Formation and evolution of binary and millisecond radio pulsars. *Phys. Rep.* 203, 1–124. doi:10.1016/0370-1573(91)90064-S.

- Bogdanov, S., et al., 2019. Constraining the Neutron Star Mass–Radius Relation and Dense Matter Equation of State with NICER. II. Emission from Hot Spots on a Rapidly Rotating Neutron Star. *Astrophys. J.* 887, L26. doi:...
- Boller, T., Haberl, F., Voges, W., Piro, L., Heise, J., 1997. New X-Ray Burster. *IAU Circ.* 6546, 1.
- Carpenter, G.F., Eyles, C.J., Skinner, G.K., Wilson, A.M., Willmore, A.P., 1977. New cosmic X-ray sources observed by the RMC experiment on Ariel V. *Mon. Not. R. Astron. Soc.* 179, 27P–34. doi:10.1093/mnras/179.1.27P.
- Church, M.J., Bałucińska-Church, M., 2004. Measurements of accretion disc corona size in lmx: consequences for comptonization and lmx models. *Mon. Not. R. Astron. Soc.* 348, 955–963. URL: <https://doi.org/10.1111/j.1365-2966.2004.07162.x>, doi:10.1111/j.1365-2966.2004.07162.x.
- Church, M.J., Gibiec, A., Bałucińska-Church, M., 2014. The nature of the island and banana states in atoll sources and a unified model for low-mass X-ray binaries. *Mon. Not. R. Astron. Soc.* 438, 2784–2797. doi:10.1093/mnras/stt2364, arXiv:1312.1823.
- Church, M.J., Halai, G.S., Bałucińska-Church, M., 2006. An explanation of the Z-track sources. *Astron. Astrophys.* 460, 233–244. doi:10.1051/0004-6361:20065035, arXiv:astro-ph/0609821.
- Done, C., Gierliński, M., Kubota, A., 2007. Modelling the behaviour of accretion flows in X-ray binaries. Everything you always wanted to know about accretion but were afraid to ask. *Astron. Astrophys. Rev.* 15, 1–66. doi:10.1007/s00159-007-0006-1, arXiv:0708.0148.
- Frank, J., King, A., Raine, D., 2002. *Accretion Power in Astrophysics*. 3rd ed., Cambridge University Press.
- Gendreau, K.C., Arzoumanian, Z., Adkins, P.W., Albert, C.L., Anders, J.F., Aylward, A.T., Baker, C.L., Balsamo, E.R., Bamford, W.A., Benegalrao, S.S., Berry, D.L., Bhalwani, S., Black, J.K., Blaurock, C., Bronke, G.M., Brown, G.L., Budinoff, J.G., Cantwell, J.D., Cazeau, T., Chen,

P.T., Clement, T.G., Colangelo, A.T., Coleman, J.S., Coopersmith, J.D., Dehaven, W.E., Doty, J.P., Egan, M.D., Enoto, T., Fan, T.W., Ferro, D.M., Foster, R., Galassi, N.M., Gallo, L.D., Green, C.M., Grosh, D., Ha, K.Q., Hasouneh, M.A., Heefner, K.B., Hestnes, P., Hoge, L.J., Jacobs, T.M., Jørgensen, J.L., Kaiser, M.A., Kellogg, J.W., Kenyon, S.J., Koennecke, R.G., Kozon, R.P., LaMarr, B., Lambertson, M.D., Larson, A.M., Lentine, S., Lewis, J.H., Lilly, M.G., Liu, K.A., Malonis, A., Manthripragada, S.S., Markwardt, C.B., Matonak, B.D., MCGinnis, I.E., Miller, R.L., Mitchell, A.L., Mitchell, J.W., Mohammed, J.S., Monroe, C.A., Montt de Garcia, K.M., Mulé, P.D., Nagao, L.T., Ngo, S.N., Norris, E.D., Norwood, D.A., Novotka, J., Okajima, T., Olsen, L.G., Onyeachu, C.O., Orosco, H.Y., Peterson, J.R., Pevear, K.N., Pham, K.K., Pollard, S.E., Pope, J.S., Powers, D.F., Powers, C.E., Price, S.R., Prigozhin, G.Y., Ramirez, J.B., Reid, W.J., Remillard, R.A., Rogstad, E.M., Rosecrans, G.P., Rowe, J.N., Sager, J.A., Sanders, C.A., Savadkin, B., Saylor, M.R., Schaeffer, A.F., Schweiss, N.S., Semper, S.R., Serlemitsos, P.J., Shackelford, L.V., Soong, Y., Struebel, J., Vezie, M.L., Villasenor, J.S., Winternitz, L.B., Wofford, G.I., Wright, M.R., Yang, M.Y., Yu, W.H., 2016. The Neutron star Interior Composition Explorer (NICER): design and development, in: den Herder, J.W.A., Takahashi, T., Bautz, M. (Eds.), *Space Telescopes and Instrumentation 2016: Ultraviolet to Gamma Ray*, p. 99051H. doi:10.1117/12.2231304.

Gierliński, M., Done, C., 2002. A comment on the colour-colour diagrams of low-mass x-ray binaries. *Mon. Not. R. Astron. Soc.* 331, L47–L50. URL: <https://doi.org/10.1046/j.1365-8711.2002.05430.x>, doi:10.1046/j.1365-8711.2002.05430.x.

Hasinger, G., van der Klis, M., 1989. Two patterns of correlated X-ray timing and spectral behaviour in low-mass X-ray binaries. *Astron. Astrophys.* 225, 79–96.

HI4PI Collaboration, Ben Bekhti, N., Flöer, L., Keller, R., Kerp, J., Lenz, D., Winkel, B., Bailin, J., Calabretta, M.R., Dedes, L., Ford, H.A., Gibson, B.K., Haud, U., Janowiecki, S., Kalberla, P.M.W., Lockman, F.J., McClure-Griffiths, N.M., Murphy, T., Nakanishi, H., Pingel, N.M., Stanimirović, S., Stein, Y., Stil, J.M., Taylor, A.R., Tian, W.W., Venzmer, M.S., Walsh, A.J., 2016. Hi4pi: A full-sky h i survey based on ebhis and gass. *Astron. Astrophys.* 594, A116. doi:10.1051/0004-6361/201629178.

- Inogamov, N.A., Sunyaev, R.A., 1999. Spread of matter over a neutron-star surface during disk accretion. *Astronomy Letters* 25, 269–293. doi:10.48550/arXiv.astro-ph/9904333, arXiv:astro-ph/9904333.
- in't Zand, J.J.M., Bassa, C.G., Jonker, P.G., Keek, L., Verbunt, F., Méndez, M., Markwardt, C.B., 2008. An X-ray and optical study of the ultracompact X-ray binary A 1246-58. *Astron. Astrophys.* 485, 183–194. doi:10.1051/0004-6361:200809361, arXiv:0804.2666.
- Jonker, P.G., in't Zand, J.J.M., Méndez, M., van der Klis, M., 2007. Detection of a 1258-Hz high-amplitude kilohertz quasi-periodic oscillation in the ultracompact X-ray binary 1A 1246-588. *Mon. Not. R. Astron. Soc.* 378, 1187–1190. doi:10.1111/j.1365-2966.2007.11854.x, arXiv:0704.1741.
- van der Klis, M., 2004. A review of rapid x-ray variability in x-ray binaries. arXiv arXiv:astro-ph/0410551.
- Kolehmainen, M., Done, C., Díaz Trigo, M., 2013. The soft component and the iron line as signatures of the disc inner radius in galactic black hole binaries. *Mon. Not. R. Astron. Soc.* 437, 316–326. URL: <https://doi.org/10.1093/mnras/stt1886>, doi:10.1093/mnras/stt1886.
- Lin, D., Remillard, R.A., Homan, J., 2007. Evaluating spectral models and the x-ray states of neutron star x-ray transients. *Astrophys. J.* 667, 1073–1086. doi:10.1086/521181.
- Ludlam, R.M., et al., 2018. NICER Discovers the Ultracompact Orbit of the Accreting Millisecond Pulsar IGR J17062-6143. *Astrophys. J.* 858, L5. doi:...
- Madsen, K.K., Harrison, F.A., Markwardt, C.B., et al., 2017. Calibration of the nuclear spectroscopic telescope array. *Astron. J.* 153, 2. doi:10.3847/1538-3881/153/1/2.
- Matsuoka, M., Kawasaki, K., Ueno, S., Tomida, H., Kohama, M., Suzuki, M., Adachi, Y., Ishikawa, M., Mihara, T., Sugizaki, M., Isobe, N., Nakagawa, Y., Tsunemi, H., Miyata, E., Kawai, N., Kataoka, J., Morii, M., Yoshida, A., Negoro, H., Nakajima, M., Ueda, Y., Chujo, H., Yamaoka, K., Yamazaki, O., Nakahira, S., You, T., Ishiwata, R., Miyoshi, S., Eguchi, S., Hiroi, K., Katayama, H., Ebisawa, K., 2009. The MAXI Mission on the ISS:

- Science and Instruments for Monitoring All-Sky X-Ray Images. *Publ. Astron. Soc. Jpn.* 61, 999. doi:10.1093/pasj/61.5.999, arXiv:0906.0631.
- Misra, R., Roy, J., Yadav, J.S., 2021. An alternative scheme to estimate AstroSat/LAXPC background for faint sources. *Journal of Astrophysics and Astronomy* 42, 55. doi:10.1007/s12036-021-09734-2, arXiv:2102.06402.
- Mitsuda, K., Inoue, H., Koyama, K., Makishima, K., Matsuoka, M., Ogawara, Y., Suzuki, K., Tanaka, Y., Hirano, T., 1984. Energy spectra of low-mass binary x-ray sources observed from tenma. *Publ. Astron. Soc. Japan* 36, 741–759.
- Mitsuda, K., Inoue, H., Nakamura, N., Tanaka, Y., 1989. Spectral variation of luminous x-ray sources in globular clusters. *Publ. Astron. Soc. Japan* 41, 97–118.
- Piro, L., Heise, J., Jager, R., Feroci, M., D’Andreta, G., Spoliti, G., Coletta, A., Muller, H., Ricci, D., 1997. *New X-Ray Burster*. IAU Circ. 6538, 2.
- Putha, K.G., Bhargava, Y., Bhattacharyya, S., 2024. Probing outbursts of the transient neutron star low-mass X-ray binary Aql X-1 with NICER: a study of spectral evolution. *Mon. Not. R. Astron. Soc.* 532, 3961–3971. doi:10.1093/mnras/stae1711, arXiv:2407.08163.
- Remillard, R.A., McClintock, J.E., 2006. X-ray properties of black-hole binaries. *Annu. Rev. Astron. Astrophys.* 44, 49–92. doi:10.1146/annurev.astro.44.051905.092532.
- Shidatsu, M., Tachibana, Y., Yoshii, T., Negoro, H., Kawamuro, T., Iwakiri, W., Nakahira, S., Makishima, K., Ueda, Y., Kawai, N., Serino, M., Kennea, J., 2017. Discovery of the New X-Ray Transient MAXI J1807+132: A Candidate of a Neutron Star Low-mass X-Ray Binary. *Astrophys. J.* 850, 155. doi:10.3847/1538-4357/aa93f0, arXiv:1710.03371.
- Singh, K.P., Stewart, G.C., Chandra, S., Mukerjee, K., Kotak, S., Beardmore, A.P., Chitnis, V., Dewangan, G.C., Bhattacharyya, S., Mirza, I., Kamble, N., Navalkar, V., Shah, H., Vishwakarma, S., Koyande, J., 2016. In-orbit performance of SXT aboard AstroSat, in: den Herder, J.W.A., Takahashi, T., Bautz, M. (Eds.), *Space Telescopes and Instrumentation 2016: Ultraviolet to Gamma Ray*, p. 99051E. doi:10.1117/12.2235309.

- Singh, K.P., Stewart, G.C., Westergaard, N.J., Bhattacharayya, S., Chandra, S., Chitnis, V.R., Dewangan, G.C., Kothare, A.T., Mirza, I.M., Mukerjee, K., Navalkar, V., Shah, H., Abbey, A.F., Beardmore, A.P., Kotak, S., Kamble, N., Vishwakarama, S., Pathare, D.P., Risbud, V.M., Koyande, J.P., Stevenson, T., Bicknell, C., Crawford, T., Hansford, G., Peters, G., Sykes, J., Agarwal, P., Sebastian, M., Rajarajan, A., Nagesh, G., Narendra, S., Ramesh, M., Rai, R., Navalgund, K.H., Sarma, K.S., Pandiyan, R., Subbarao, K., Gupta, T., Thakkar, N., Singh, A.K., Bajpai, A., 2017. Soft X-ray Focusing Telescope Aboard AstroSat: Design, Characteristics and Performance. *Journal of Astrophysics and Astronomy* 38, 29. doi:10.1007/s12036-017-9448-7.
- Singh, K.P., Tandon, S.N., Agrawal, P.C., Antia, H.M., Manchanda, R.K., Yadav, J.S., Seetha, S., Ramadevi, M.C., Rao, A.R., Bhattacharya, D., Paul, B., Sreekumar, P., Bhattacharyya, S., Stewart, G.C., Hutchings, J., Annapurni, S.A., Ghosh, S.K., Murthy, J., Pati, A., Rao, N.K., Stalin, C.S., Girish, V., Sankarasubramanian, K., Vadawale, S., Bhalerao, V.B., Dewangan, G.C., Dedhia, D.K., Hingar, M.K., Katoch, T.B., Kothare, A.T., Mirza, I., Mukerjee, K., Shah, H., Shah, P., Mohan, R., Sangal, A.K., Nagabhusana, S., Sriram, S., Malkar, J.P., Sreekumar, S., Abbey, A.F., Hansford, G.M., Beardmore, A.P., Sharma, M.R., Murthy, S., Kulkarni, R., Meena, G., Babu, V.C., Postma, J., 2014. ASTROSAT mission, in: Takahashi, T., den Herder, J.W.A., Bautz, M. (Eds.), *Space Telescopes and Instrumentation 2014: Ultraviolet to Gamma Ray*, p. 91441S. doi:10.1117/12.2062667.
- Suleimanov, V., Poutanen, J., Werner, K., 2012. X-ray bursting neutron star atmosphere models using an exact relativistic kinetic equation for compton scattering. *Astron. Astrophys.* 545, A120. doi:10.1051/0004-6361/201219480.
- Sunyaev, R.A., Titarchuk, L.G., 1980. Comptonization of X-Rays in Plasma Clouds - Typical Radiation Spectra. *Astron. Astrophys.* 86, 121–138.
- van Doesburgh, M., van der Klis, M., Morsink, S.M., 2018. The highest frequency kHz QPOs in neutron star low-mass X-ray binaries. *Mon. Not. R. Astron. Soc.* 479, 426–434. doi:10.1093/mnras/sty1404, arXiv:1805.11361.

- van Haften, L. M., Nelemans, G., Voss, R., Wood, M. A., Kuijpers, J., 2012. The evolution of ultracompact x-ray binaries. *Astron. Astrophys.* 537, A104. URL: <https://doi.org/10.1051/0004-6361/201117880>, doi:10.1051/0004-6361/201117880.
- Verner, D.A., Ferland, G.J., Korista, K.T., Yakovlev, D.G., 1996. Atomic Data for Astrophysics. II. New Analytic FITS for Photoionization Cross Sections of Atoms and Ions. *Astrophys. J.* 465, 487. doi:10.1086/177435, arXiv:astro-ph/9601009.
- White, N.E., Stella, L., Parmar, A.N., 1988. The X-Ray Spectral Properties of Accretion Disks in X-Ray Binaries. *Astrophys. J.* 324, 363. doi:10.1086/165901.
- Wilms, J., Allen, A., McCray, R., 2000. On the Absorption of X-Rays in the Interstellar Medium. *Astrophys. J.* 542, 914–924. doi:10.1086/317016, arXiv:astro-ph/0008425.
- Yadav, J.S., Agrawal, P.C., Antia, H.M., Chauhan, J.V., Dedhia, D., Katoch, T., Madhwani, P., Manchanda, R.K., Misra, R., Pahari, M., Paul, B., Shah, P., 2016. Large Area X-ray Proportional Counter (LAXPC) instrument onboard ASTROSAT, in: den Herder, J.W.A., Takahashi, T., Bautz, M. (Eds.), *Space Telescopes and Instrumentation 2016: Ultraviolet to Gamma Ray*, p. 99051D. doi:10.1117/12.2231857.
- Yadav, J.S., Agrawal, P.C., Antia, H.M., Manchanda, R.K., Paul, B., Misra, R., 2017. Large Area X-ray Proportional Counter instrument on AstroSat. *Current Science* 113, 591. doi:10.18520/cs/v113/i04/591-594, arXiv:1705.06440.
- Zdziarski, A.A., Johnson, W.N., Magdziarz, P., 1996. Broad-band γ -ray and X-ray spectra of NGC 4151 and their implications for physical processes and geometry. *Mon. Not. R. Astron. Soc.* 283, 193–206. doi:10.1093/mnras/283.1.193, arXiv:astro-ph/9607015.
- Zhang, L., Méndez, M., García, F., Zhang, Y., Ma, R., Altamirano, D., Yang, Z.X., Ma, X., Tao, L., Huang, Y., Jia, S., Zhang, S.N., Qu, J., Song, L., Zhang, S., 2023. Type-A quasi-periodic oscillation in the black hole transient MAXI J1348-630. *Mon. Not. R. Astron. Soc.* 526, 3944–3950. doi:10.1093/mnras/stad3062, arXiv:2310.04208.

Życki, P.T., Done, C., Smith, D.A., 1999. The 1989 May outburst of the soft X-ray transient GS 2023+338 (V404 Cyg). *Mon. Not. R. Astron. Soc.* 309, 561–575. doi:10.1046/j.1365-8711.1999.02885.x, arXiv:astro-ph/9904304.